

Size-Dependent Mixing Characteristics of Volatile and Nonvolatile Components in Diesel Exhaust Aerosols

HIROMU SAKURAI, KIHONG PARK, AND
PETER H. MCMURRY*

*Particle Technology Laboratory, Department of Mechanical Engineering, University of Minnesota,
Minneapolis, Minnesota 55455*

DARRICK D. ZARLING AND
DAVID B. KITTELSON

*Center for Diesel Research, Department of Mechanical Engineering, University of Minnesota,
Minneapolis, Minnesota 55455*

PAUL J. ZIEMANN†

*Air Pollution Research Center, University of California,
Riverside, California 92521*

Mixing characteristics of particles of different volatilities from a diesel engine were studied with two tandem differential mobility analyzers (TDMAs) and an aerosol particle mass analyzer (APM). In both TDMA systems, a heater was located in the aerosol path between the first and second DMAs. Diesel exhaust particles that were size-selected in the first DMA were passed through the heater, and the change in particle size due to loss of volatile components was determined by the second DMA. On the basis of the volatility measurements, the particles could be separated into two overlapping modes that varied in peak diameter and magnitude depending on the engine operating conditions. Particles in the smaller size mode were almost completely volatile, while those in the larger size mode contained a nonvolatile core. The TDMA data inversion technique used here allowed accurate determination of the mixing ratios of the two types of particles. These data were in turn used to validate a simple fitting method that uses two log-normal curves to obtain the mixing ratios. In some experiments, the APM was used downstream of a TDMA to directly measure the particle mass loss due to evaporation. The loss determined by the TDMA–APM system was significantly greater than that calculated from mobility size changes measured solely with the TDMA. The TDMA–APM results were used to calculate the size-dependent mass concentrations of volatile and nonvolatile components for particles in the size range from 70 to 200 nm.

Introduction

Recent epidemiological studies have shown a positive association between short-term exposure to elevated levels

of ambient fine particulate matter (diameter $<2.5\ \mu\text{m}$) and increased morbidity and mortality (1–3). However, the mechanisms by which particles may cause adverse health effects are not understood. It is not yet clear to what extent the effects depend on aerosol mass, surface area, number concentrations, or specific physical and chemical properties such as size, state (i.e., liquid or solid), and composition (4, 5). Hypotheses regarding aerosol properties that could lead to human physiological or toxic responses have been proposed (6), and research is underway in a number of laboratories to test them. These hypotheses include the possibilities that ultrafine particles (diameter $<100\ \text{nm}$) may have physiological effects that are greater than expected for their typically low mass concentrations, that certain organic compounds and metals may be toxic, and that soot (elemental carbon) particles or their adsorbed material may stimulate a toxic response.

Diesel exhaust particles are attracting significant attention with regards to their potential health effects (7–9) since they can be formed in high concentrations as ultrafine particles and can contain high levels of organic compounds and soot. The recent literature includes a number of studies on the physical and chemical properties of diesel particles (10). The size distribution can range from $<10\ \text{nm}$ to $>1\ \mu\text{m}$ and is often bimodal with distinct accumulation and nuclei (or nanoparticle) modes. The accumulation mode is found in the size range from ~ 30 to $1000\ \text{nm}$ and contains most of the particle mass ($>80\%$). The nuclei mode consists of particles in the diameter range from a few nanometers to ~ 30 – $100\ \text{nm}$ and under many conditions dominates the particle number ($>90\%$) while the mass of this mode is usually less than 1% but may be larger. The position of the boundary between the nuclei and accumulation modes varies and depends on the relative sizes of the modes. Formation of nuclei-mode particles occurs during exhaust dilution and cooling and is highly sensitive to the dilution conditions (e.g., temperature and mixing dynamics) (11, 12) as well as engine type, fuel, oil, and after-treatment used in the exhaust line.

The major components of diesel particles include elemental carbon, semivolatile organics, ash, and sulfates (10, 13). Particles in the accumulation mode contain soot (i.e., agglomerates of nonvolatile, elemental carbon particles) with associated adsorbed semivolatile materials. Particles in the nuclei mode are known to be volatile typically, as has been shown by using a catalytic stripper (14) and a thermodesorber (or thermodenuder) (15, 16) to observe the disappearance of the nuclei mode when the particles were heated at 200 – $300\ ^\circ\text{C}$. Recently, we studied particles from a heavy-duty diesel engine and found that the major volatile constituent of nanoparticles and accumulation-mode particles was predominantly hydrocarbons from unburned lubricating oil (17). If there is significant metallic ash present, either from lubricating oil or fuel additives, solid ash particles may appear in the nuclei mode (18–22).

These studies of the physical and chemical properties of diesel particles, however, did not provide detailed information on the distribution of the different types of diesel exhaust particles present in different size ranges, nor did they provide information on the relative amounts of organic compounds, soot, ash, sulfates, etc. in particles of different sizes. It is important to understand the heterogeneous nature of diesel exhaust particles in order to better understand their health effects and to develop emissions control strategies. Also, such information provides insights into measurement methods. In the present work, we report on measurements of the mixing properties of diesel exhaust particles conducted with the

* Corresponding author phone: (612)624-2817; fax: (612)626-1854; e-mail: mcmurry@me.umn.edu.

† Also in the Department of Environmental Sciences, Department of Chemistry, and Environmental Toxicology Graduate Program, University of California, Riverside.

TABLE 1. Summary of the Setup of the Nano and Long SMPS, Nano TDMA, and Long TDMA–APM Systems

	Nano SMPS	Long SMPS	Nano TDMA	Long TDMA–APM
DMA column(s)	TSI Nano DMA 3085	TSI 3071 equivalent	2 TSI Nano DMA 3085s	2 TSI 3071 equivalents
CPC	TSI 3025 UCPC	TSI 3010 CPC	TSI 3025A UCPC	TSI 3760 CPC
size range (nm)	3–50	10–280	3–50	15–200
dilution ratios ^a	56; 14 × 4 (80; 20 × 4)	378; 14 × 27 (540; 20 × 27)	14 (20)	378; 14 × 27 (540; 20 × 27)
residence time in VRTDS (s)	1.8	1.8	1.8	1.8
temperatures in VRTDS (°C)				
at 20% load	27–28	27–28	27–28	27–28
at 30% load	35–37	35–37	35–37	35–37
residence time(s) in sampling line after VRTDS (s) ^b	0.5	0.3; 0.2	0.5	0.3; 4

^a The numbers before and after the semicolon are the overall dilution ratio and the dilution ratios at individual stages, respectively. The numbers in the parentheses are those with the engine operating on CA fuel at 35% load. ^b The residence times before and after the semicolon indicate those before and after secondary dilution, respectively.

tandem differential mobility analyzer (TDMA) technique based on volatility, which is similar to the technique previously reported (23, 24) and has been applied to laboratory-generated particles (25, 26), ambient particles (27), and combustion-generated particles including those from diesel exhaust (27–29). These measurements illustrated the capacity of the volatility TDMA technique to study size-dependent mixing characteristics of particles and materials with different volatilities. Our measurements of diesel exhaust particles covered a wider range of sizes than has been previously reported. Volatile particles were analyzed with a TDMA system that was able to detect particles as small as 3 nm; therefore, the existence of nonvolatile residues in volatile nuclei-mode particles was investigated down to that size. We also used an aerosol particle mass analyzer (APM) (30, 31) to measure changes in mass upon heating, which provided especially valuable insights into the volatile fraction of irregularly shaped particles. These measurements enabled us to quantify, for given engine operating conditions, (i) the size-dependent relative proportions between volatile particles and particles containing volatile material with a nonvolatile core and (ii) the size-dependent mass fractions of volatile and nonvolatile materials on the particles with a nonvolatile core. We were also able to validate a fitting method to obtain the mixing ratios of the two types of particles and to reconstruct the overall size distribution by superposing them. Furthermore, these results were used to calculate the mass concentration distributions of volatile and nonvolatile components. Overall, the ability of the TDMA and TDMA–APM techniques to characterize diesel particle mixtures by volatility was clearly demonstrated.

Experimental Section

A summary of the measurement systems used in this study and their sampling settings is given in Table 1, and more detailed descriptions of them are provided below.

Diesel particle size distributions were measured using two scanning mobility particle sizers (SMPSs) (32). One SMPS system consisted of a Po-210 bipolar charger, a DMA of a conventional column length similar in design to the TSI model 3071 (33, 34), and a TSI model 3010 condensation particle counter (CPC) for 10–280-nm particles (Long SMPS), while the other SMPS consisted of a Po-210 bipolar charger, TSI Nano DMA (35), and TSI ultrafine CPC (36) for 3–50-nm particles (Nano SMPS).

Diesel particle volatility was measured using a tandem differential mobility analyzer equipped with Nano DMA columns and a TSI ultrafine CPC for the particle size range from 3 to 50 nm (Nano TDMA) and another TDMA system with DMAs of a conventional column length and a TSI model 3760 CPC for the particle size range from 15 to 200 nm, which was equipped with an APM (30, 31) (Long TDMA–APM).

The APM is a prototype that was manufactured by Kanomax Japan Inc. In the Nano TDMA, the aerosol and sheath airflow rates were maintained at 1.5 and 15 L min^{−1} in both Nano DMAs. In the Long TDMA–APM, the aerosol flow rate was 1.5 L min^{−1} throughout the system, and the sheath airflow rates were 10 and 6.9 L min^{−1} in the first and second DMAs (DMA1 and DMA2), respectively. In each TDMA system, particles first passed through a Po-210 bipolar charger and into DMA1, which was used to select monodisperse particles. This aerosol then entered a heated tube set at a constant temperature in which volatile aerosol components evaporated. Particles passing through the heated tube then entered DMA2 and the CPC (the APM was bypassed in the Long TDMA–APM in this case) and were re-sized to determine the change in size due to evaporation. During TDMA measurements, CPC concentrations were measured at a discrete set of DMA2 voltages (rather than sweeping DMA2 voltages), and the voltage was always stepped upward. For each heater temperature, the size distribution at the exit of the heater was calculated from the relationship between the DMA2 voltage V_2 and CPC concentration N_2 through a data inversion procedure that is described in the next section.

The heaters, similar to that described by Orsini et al. (24), consisted of a 1/4 in. o.d., ~50 cm long stainless steel tube wrapped with a 200-W heating tape. The heater temperature was measured by a thermocouple inserted into the heated tube from its downstream end so that the measuring tip of the thermocouple was located near the end of the heated section off the tube wall. This temperature was used as the representative temperature of the heater in this study. The heater temperature was controlled within ± 1 °C of the target temperature. The temperature range used was from ~25–30 °C (room temperature) to ~450 °C. The estimated average residence time of particles in the heaters was ~0.25 s at room temperature. After the heated section, particles passed through a stainless steel tube (60 and 150 cm long for the Nano and Long TDMA, respectively), which was naturally cooled by room air, before entering DMA2. There was a concern that re-condensation or re-nucleation of volatile species that evaporated from particles might occur in the cooling section and affect size distribution measurements. To avoid this problem, others have used aerosol heating devices that have a gas adsorber after the heating section (29, 37). We, instead, carried out an experiment which convinced us that re-condensation and re-nucleation was negligible in our study. This experiment involved repeating volatilization measurements after diluting the aerosol by about a factor of 10. We reasoned that if re-condensation or re-nucleation were significant, then particles should evaporate more in the diluted aerosol than in the undiluted aerosol. In fact, results for the diluted and undiluted aerosol were identical. Since only charged and size-classified particles

exited DMA1 and entered the heated tube, the concentration of evaporated species in the cooling section was probably too low to cause re-condensation and re-nucleation. Orsini et al. also demonstrated with laboratory-generated aerosols that recondensation was negligible in their volatility TDMA system (24).

Another mode of operation of the Long TDMA-APM was to use the APM to measure the mass of particles exiting DMA2. Detailed descriptions are given elsewhere for the APM (30) and the Long TDMA-APM (31, 38). Briefly, the APM consists of two 250-mm-tall cylindrical electrodes that rotate at the same angular speed. The inner radius of the outer cylinder is 63 mm, and the outer radius of the inner cylinder is 60 mm. Charged, mobility-classified aerosol particles are introduced axially into the annular gap between the electrodes and rotate at the same speed as the electrodes as they travel downward through the gap. A negative voltage was applied to the inner electrode while the outer electrode was grounded, which generated a radial electric field. Particles in the gap experienced an outward centrifugal force and an inward electrostatic force since the particles from the Long TDMA were positively charged. When these forces were balanced, particles penetrated through the gap without impacting on the electrodes and were detected by the CPC. By controlling the rotation speed and voltage, the APM classifies particles of a desired mass. It should be noted that mass classification by the APM is independent of particle shape. This is in contrast to size classification by the DMA, which separates particles according to their electrical mobility, a property that depends on particle shape. In these experiments, particles that exited the heater were size-selected by Long DMA2 and then delivered to the APM for mass measurement.

The engine was a 1999 model, 6-cylinder, 10.8-L displacement, 4-cycle, heavy-duty diesel engine that produced a peak torque of 1831 N-m at 1200 rpm and 290 kW maximum power at 1800 rpm. The engine was equipped with an electronically controlled high-pressure fuel injection system representative of current heavy-duty engine practice. Experiments were performed at a constant engine speed of 1400 rpm at light and medium loads of 20% (366 N-m) and 35% (692 N-m) with either California low-sulfur fuel (CA; 96 ppm S) or U.S. EPA on-highway pump fuel (EPA; 360 ppm S) and with a commercially available 15W-40 lubricating oil for diesel engines. Diesel exhaust was diluted using a two-stage, ejector-type variable residence time dilution system (VRTDS) (12). The air used for dilution was particle-free with a very low relative humidity (~5%). The primary and secondary dilution ratios were 14:1 (20:1 at 35% engine load with CA fuel) and 27:1, respectively, which were determined from the ratio of NO_x concentrations in undiluted and diluted exhaust. Temperatures in the first stage of the VRTDS were 27–28 and 35–37 °C at the engine loads of 20% and 35%, respectively. Aerosol was sampled directly after primary dilution to maximize particle concentrations for the Nano TDMA, while the Long TDMA-APM and Long SMPS were sampled after the secondary dilution. The sample for the Nano SMPS was taken after primary dilution and was further diluted by a factor of 4 before the bipolar charger. The average residence time of diluted exhaust in the VRTDS between the first ejector and the exit tube of the VRTDS was ~1.8 s. The combination of dilution ratio, temperature, and residence time in the first stage of the VRTDS gave a condition that should favor the formation of a stable nucleation mode (12). The sample exhaust then spent ~0.5 s in transfer lines before entering the Nano SMPS and the Nano TDMA and ~0.3 s before entering the secondary dilution ejector. The sample after secondary dilution spent ~0.2 and 4 s before entering the Long SMPS and Long TDMA-APM, respectively. The time to complete a TDMA measurement at each size at a fixed heater temperature was typically 5–15 min, depending

on the width of the size distribution of heated particles and the concentration. We operated the two SMPSs repeatedly and monitored the stability of the size distribution of the sample aerosols and confirmed that the size distribution did not change significantly over many hours. When the engine operating condition or dilution condition was changed, TDMA and TDMA-APM measurements were commenced after the size distribution was stabilized.

Data Processing Procedure. The state of external mixing is obtained from volatility by determining the relative number concentrations of particles that exhibit distinctly different degrees of volatility. This requires calculating the particle size distribution function at the exit of the heater and integrating it within the size range of each distinctive volatility “mode”. Obtaining the particle size distribution function at the heater exit (referred to hereafter as n_{heater} , which is defined as dN_{heater}/dD_p where N_{heater} is the total particle number concentration at the heater exit) from the measured relationship between the DMA2 voltage (V_2) and CPC concentration (N_2) involves using the data reduction process described below.

When the DMA2 voltage is V_2 , the CPC concentration N_2 is expressed using n_{heater} as

$$N_2(V_2) = \int_0^\infty n_{\text{heater}}(D_p) \eta_{\text{heater}-2}(D_p) \Omega_2(D_p, V_2) \eta_2(D_p) \eta_{2-\text{CPC}}(D_p) \zeta_{\text{CPC}}(D_p) dD_p \quad (1)$$

where $\eta_{\text{heater}-2}(D_p)$ is the particle transmission efficiency through the plumbing tube after the heater up to the inlet of DMA2, $\Omega_2(D_p, V_2)$ is the transfer function of DMA2 (33), $\eta_2(D_p)$ is the transmission efficiency of DMA2, $\eta_{2-\text{CPC}}(D_p)$ is the transmission efficiency through the tube between DMA2 and the CPC, and $\zeta_{\text{CPC}}(D_p)$ is the detection efficiency of the CPC. Note that the transmission efficiency of DMA2 is separated from the DMA transfer function in this expression. Particles that were smaller than 50 nm when classified by DMA1 were assumed to be all singly charged because of very low probabilities to acquire multiple charges for particles that affect this size range under the bipolar charging condition. For particles above 50 nm, the effect of multiply charged particles was evaluated and found insignificant in all cases. We assumed that particles did not lose the charge upon heating and evaporation of volatile compounds. The terms $\eta_{\text{heater}-2}$ and $\eta_{2-\text{CPC}}$ were estimated by considering solely diffusional deposition of particles onto wall surfaces in straight tubes (ignoring bends and fittings). Thermophoretic losses downstream of the heater were assumed to be negligible. This is based on the observation in an experiment where the concentration of 10-nm sodium chloride particles decreased only by ~10% when the heater temperature was varied from room temperature to 450 °C, which is different from the findings by Orsini et al. (24). The diffusion-broadened DMA transfer function Ω_2 was calculated using the expression derived by Stolzenburg (39). The DMA2 transmission efficiencies, η_2 , were obtained from Chen et al. (35) for the Nano DMA and from Kousaka et al. (40) for the long-column DMA. Corrections for this transmission efficiency was found very important in determining the relative concentrations between modes of very different volatilities. The CPC detection efficiencies, ζ_{CPC} , were obtained from Kesten et al. (41) for the UCPC and from Zhang and Liu (42) for the 3760 CPC. The integrand of eq 1 is nonzero only in the narrow diameter range [designated here as $D_p^* - \Delta D_p^* < D_p < D_p^* + \Delta D_p^*$ where $D_p^* = D_p^*(V_2)$ is the centroid diameter of the DMA2 transfer function and ΔD_p^* is its half width] where the transfer function Ω_2 is nonzero. Since $\eta_{\text{heater}-2}$, η_2 , and, $\eta_{2-\text{CPC}}$ do not vary significantly for this small interval of D_p , eq 1 can be approximated as

$$N_2(V_2) = \eta_{\text{heater}-2}(D_p^*)\eta_2(D_p^*)\eta_{2-\text{CPC}}(D_p^*) \int_{D_p^* - \Delta D_p^*}^{D_p^* + \Delta D_p^*} n_{\text{heater}}(D_p)\Omega_2(D_p, V_2)\zeta_{\text{CPC}}(D_p) dD_p^* \quad (2)$$

The CPC detection efficiency term ζ_{CPC} is left in the integral, so this equation can be used even near the detection cutoff diameter of the CPC where the detection efficiency varies strongly with size. The distribution function n_{heater} cannot be taken out of the integral as is usually done with SMPS inversions since this distribution function may vary significantly over the range of the integral (43), which is especially true for the cases when particles did not shrink significantly from the initial size and the particle size distribution is as wide as or only slightly wider than the DMA2 transfer function. Rader and McMurry (44) and Stolzenburg and McMurry (45) demonstrated methods to solve eq 2 rigorously for the case that the particle size distribution entering DMA2 consists of one or two “modes” that were simply shifted by a constant factor from the distribution leaving DMA1. However, because the evaporated diesel particles were not always found in one or two well-defined peaks but instead were distributed across a wide range of particle sizes, a data reduction method with fewer restrictions on the transformation needed to be used here. Iterative TDMA inversion techniques to solve eq 2 have employed various types of inversion algorithms (46, 47). In this study, the inversion algorithm by Markowski (48) was used. It should be noted that the inversion could not provide any useful information on n_{heater} for sizes below the CPC detection limit (~ 3 nm for the Nano TDMA and ~ 15 nm for the Long TDMA).

The total particle number concentration after the heater (N_{heater}), which was calculated from the inverted size distribution (n_{heater}), was used as an indicator to test the accuracy of the overall correction for the size-dependent efficiencies (i.e., $\eta_{\text{heater}-2}$, η_2 , $\eta_{2-\text{CPC}}$, and ζ_{CPC}) and the assumptions that thermophoretic particle losses and loss of particle charge were negligible. This was done by comparing the total concentrations at elevated temperatures with those at room temperature. For both Nano and Long TDMA measurements, the calculated total concentration showed nearly 100% recovery in most cases with random fluctuations of the magnitude of $\sim 20\%$, which were possibly due to fluctuations of the engine exhaust. This good agreement supports the validity of the estimates and assumptions we made above on losses and efficiencies. However, when particles became as small as 3–6 nm at the heater temperature of 300 °C and above in Nano TDMA measurements, only 50–70% of particles were recovered. We have not determined the reason for this decrease at small sizes and high temperatures. It could be that some particles evaporated below the minimum detectable size (23) or that, in those size and temperature ranges, losses due to deposition to tube walls and charge losses are greater than were estimated in our inversion algorithm. Higgins et al. reported that charge loss was observed when particles of 40 nm and larger were heated at above 500 °C between the two DMAs in their TDMA experiment on oxidation of soot (49). This implies that, although their particle size and temperature ranges were different from ours, loss of particle charge upon heating cannot be ruled out and may have occurred in our experiment.

Results and Discussion

Particle Size Distributions. Figure 1 shows the size distributions of diesel exhaust particles for the conditions used in this study: (A) 20% load with CA fuel, (B) 35% load with CA fuel, and (C) 35% load with EPA fuel. Note that the distributions are for particles sampled after primary dilution. In order to create a composite size distribution curve from

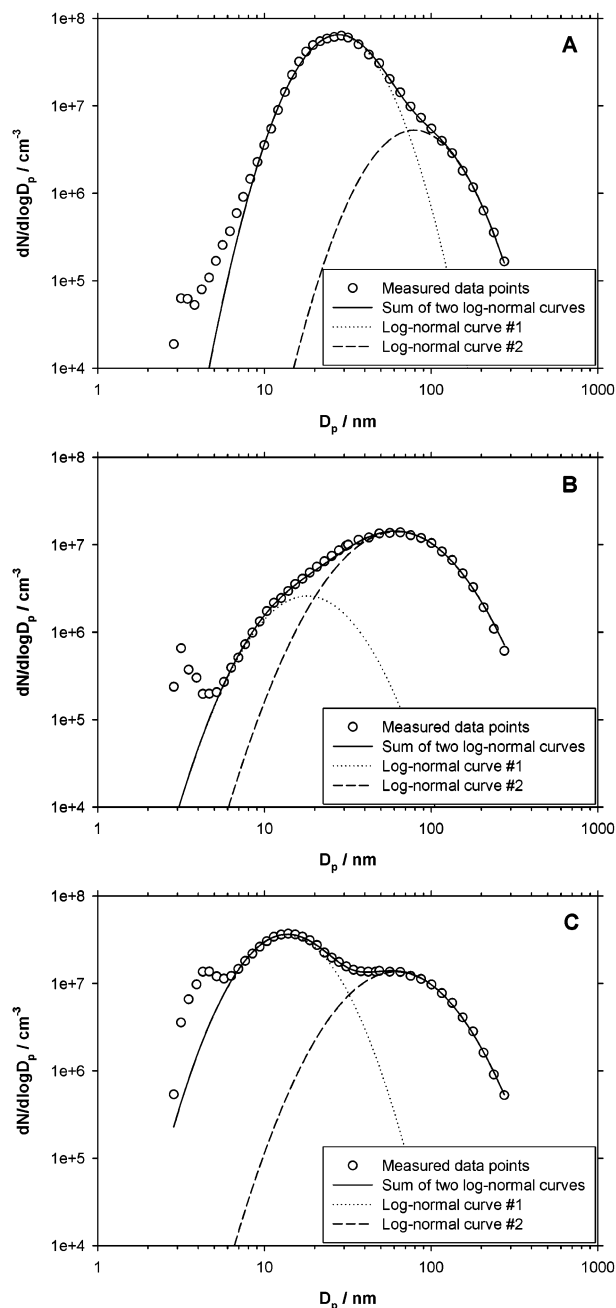


FIGURE 1. Particle size distributions of diesel exhaust aerosols formed with the engine operating on (A) CA fuel at 20% engine load, (B) CA fuel at 35% load, and (C) EPA fuel at 35% load, measured after primary dilution. The curves were obtained by fitting with two log-normal distributions using the parameters given in the text.

data taken by the two SMPS systems, data were corrected for secondary dilution. The shape of the two SMPS size distribution curves agreed fairly well in the size range between 20 and 50 nm even though the two SMPSs sampled from different dilution stages, while the agreement in the concentrations was not consistent with the estimated dilution ratios. The curves of the two SMPSs were forced to align in the size range from 20 to 50 nm, which was accomplished by adjusting a multiplying factor to shift the Long SMPS curve upward in the size distribution plot. Then the curve in the size range of 3–30 nm of the Nano SMPS curve and that of 30–280 nm were combined. The original size distribution curves used to create the composite curves shown in Figure 1 and the multiplying factors used in each plot are provided in the Supporting Information. We were not able to identify

the source of the nonunity multiplying factors, which ranged from 3.6 to 4.8. Perhaps they may have arisen due to uncertainties in the dilution ratios. In Figure 1A, the total particle number concentration between 3 and 280 nm was 3.3×10^7 particles cm^{-3} , and the mode diameter occurred at 28 nm. Under this condition, the number concentration was dominated by particles of the nuclei mode. The size distribution did not have a distinct accumulation mode peak but only a shoulder starting at ~ 70 –80 nm. The data points between 10 and 280 nm were fitted by using two log-normal distribution functions, which are also plotted in Figure 1A. This method has been used previously with success to fit the bimodal structure of diesel exhaust particle size distributions (20). The validity of fitting the accumulation mode of diesel exhaust with a log-normal function has been demonstrated by Harris and Maricq (50). The two log-normal distributions had geometric mean diameters, geometric standard deviations, and total number concentrations of 28 nm, 1.53, and 3.0×10^7 particles cm^{-3} for the nuclei mode and 79 nm, 1.60, and 2.7×10^6 particles cm^{-3} for the accumulation mode, respectively. The sum of the two log-normal distributions fit the experimental data very well, especially in the size range where the nuclei and accumulation modes merge. The size distributions shown in Figure 1B,C were also fitted with two log-normal functions. The geometric mean diameters, geometric standard deviations, and total number concentrations of the two modes were 20 and 61 nm, 1.76 and 1.83, and 1.8×10^6 and 9.3×10^6 particles cm^{-3} for 35% load with CA fuel (Figure 1B) and 14 and 62 nm, 1.63 and 1.80, and 1.9×10^7 and 8.8×10^6 particles cm^{-3} for 35% load with EPA fuel (Figure 1C), respectively.

Characteristics of the size distributions and their dependence on operating conditions are consistent with those previously reported (20, 51). When the engine load was increased while using the same fuel (Figure 1A,B), the intensity of the nuclei mode decreased while that of the accumulation mode increased. The standard deviation of the accumulation mode was greater at the higher engine load. When fuel with a higher sulfur content was used at the same engine load (Figure 1B,C), the intensity of the nuclei mode increased while that of the accumulation mode did not change significantly. Surprisingly, a small third mode was observed below 10 nm, which was most prominent with EPA fuel at 35% load (Figure 1C). We do not know the nature of these particles, but metals from the lubricating oil may play a role. Recent single-particle mass spectrometric measurements suggest that the smallest particles emitted by diesel engines are relatively enriched with metal compounds formed from metals in the fuel or lubricating oil (18).

External Mixing of Particles of Different Volatilities.

Figure 2 shows results of Long TDMA volatility experiments for diesel particles with the initial diameter (the DMA1 diameter) of 70 nm, formed using CA fuel at 20% load. When these particles were heated at 70 °C, the peak in the monomodal size distribution simply shifted to 66 nm due to evaporation of volatile components. When the heater temperature was increased to 90 °C, although one peak remained at 65 nm, the distribution broadened and a second mode appeared at 54 nm. As the heater temperature was increased to 110 °C and higher, particles in the second mode continued to shrink, eventually dropping below the detection limit of 15 nm at 190 °C. These observations indicate that the 70-nm diesel exhaust aerosol was an external mixture of two types of particles with very different volatilities. The particles that shrank slightly to 65 nm and then stopped were probably composed of a large nonvolatile soot core coated with volatile organic matter, while the mode that appeared at 90 °C and then continued to shrink at higher temperatures was associated with particles mostly composed of volatile compounds. We will hereafter refer to these two modes as “less

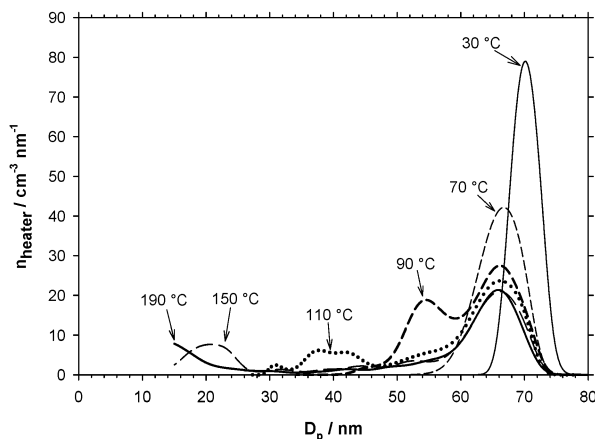


FIGURE 2. Evaporation profiles of initially 70-nm diesel particles formed with the engine operating on CA fuel at 20% load.

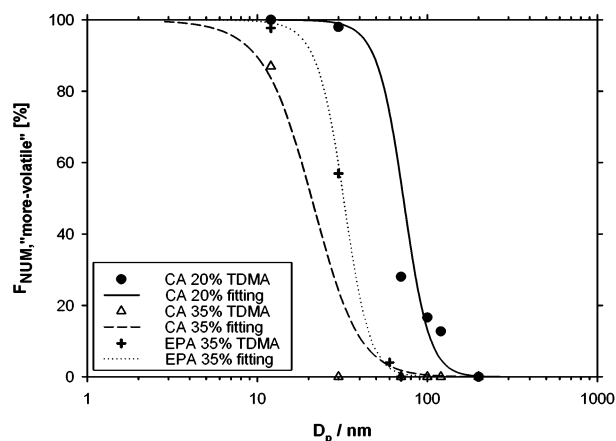


FIGURE 3. Size-dependent number fractions of “more volatile” diesel particles formed with the engine operating on CA and EPA fuels at different loads. The curve shows “more volatile” fractions estimated from the log-normal fitting procedure shown in Figure 1.

volatile” and “more volatile” particles. It should be noted that, in this study, the criterion for a substance to be defined as volatile is that its vapor pressure is comparable to or greater than those of the major hydrocarbon compounds in engine oil (17). To describe this in a quantitative manner, we estimated the vapor pressure of the C32 *n*-alkane, a major constituent of engine oil, to be 4×10^{-3} Pa at 110 °C based on the method given by Lemmon and Goodwin (52). The vapor pressure of the same compound at 20 °C was estimated to be on the order of 10^{-9} Pa by extrapolating the vapor pressure curve to below the melting point (70 °C).

For the 70-nm particles, the number fraction of “more volatile” particles ($F_{\text{NUM, “more-volatile”}}$) was 28% at both 110 and 150 °C. The results of similar analyses made on particles with initial sizes of 12 and 30 nm (Nano TDMA) and 100, 120, and 200 nm (Long TDMA) are shown in Figure 3. Also plotted is a curve representing “more volatile” particle number fractions calculated from the two log-normal distribution functions shown in Figure 1A, assuming that the nuclei mode is composed of “more volatile” particles and the accumulation mode of “less volatile” particles. The mixing ratios measured with the TDMA are in good agreement with those obtained by log-normal curve fitting. The agreement for CA fuel at 35% load and for EPA fuel for 35% load is also good, with the slight discrepancy for the CA fuel at 35% possibly being due to the weaker nuclei mode and larger uncertainty in the double log-normal fitting. The curves shift to smaller particle sizes in the order of CA fuel at 20% load, EPA fuel at 35%,

and CA fuel at 35%, which reflects the decreasing relative intensities of the nuclei mode.

Volume Fractions of Volatile and Nonvolatile Compounds in “More Volatile” and “Less Volatile” Particles. The relative contributions of volatile and nonvolatile material to the volume of “more volatile” and “less volatile” particles were calculated from the change in particle size due to heating. Two techniques were used to obtain this information and then compared: one is based on TDMA measurements of the change in mobility-equivalent diameter, while the other utilizes the Long TDMA–APM to measure the change in particle mass.

In the first method, the volume fraction of the volatile material ($F_{VOL,volatile}^{TDMA}$) is calculated from the diameter change determined by the TDMA, with the assumption that the particles are spherical:

$$F_{VOL,volatile}^{TDMA} = 1 - \frac{V_{p,nonvolatile}^{TDMA}}{V_{p,initial}^{TDMA}} = 1 - \left(\frac{D_{p,nonvolatile}^{TDMA}}{D_{p,initial}^{TDMA}} \right)^3 \quad (3)$$

where $D_{p,initial}^{TDMA}$ and $V_{p,initial}^{TDMA}$ are the mobility-equivalent diameter and volume before heating, and $D_{p,nonvolatile}^{TDMA}$ and $V_{p,nonvolatile}^{TDMA}$ are the mobility-equivalent diameter and volume after heating. Temperatures of 150 and >190 °C were used for the Nano and Long TDMA, respectively, to ensure that volatile compounds were completely driven off from particles. In measurements with CA fuel at 20% load, the diameter of nonvolatile residue in “more volatile” 30-nm particles was 4 nm. For 12-nm particles, the mean diameter of the “more volatile” mode became smaller than the 3-nm detection limit of the UCPC. Although the actual size of the particles could not be determined because of the UCPC limitation, residual particles were observed even when particles were heated at 400–450 °C, and the presence of nonvolatile residues in “more volatile” particles seemed real. Although we do not know the composition of the residual particles, we think it unlikely that the residual particles were formed due to pyrolytic charring of organics in the “more volatile” particles in the heater tube, as we discussed in our recent paper (17). It should be noted that this observation of nonvolatile residues does not necessarily mean the nonvolatile species provided condensation nuclei during the formation of “more volatile” particles. For example, the nonvolatile species may have been taken into the particles after the particles were formed. For the purpose of calculations of the volatile volume fraction, since the actual residue diameter could not be measured, 3 nm was used to obtain a lower limit for the volatile volume fraction. The 15-nm detection limit of the TSI 3760 CPC was used for the nonvolatile residues of “more volatile” particles studied with the Long TDMA (i.e., 70, 100, and 120 nm diameter) although in these cases the size distribution did not show indication of the presence of nonvolatile residues. Since “more volatile” particles presumably do not contain soot agglomerates and our previous studies indicated that their composition is similar to oil (17), those particles should be nearly spherical, and the volume fraction obtained here must be fairly accurate. The volatile volume fractions of “less volatile” particles were calculated in the same way, ignoring effects that may be caused by their nonspherical shapes. For the 30-nm particles, since the size distribution of the nonvolatile core was broadly distributed up to 15 nm, 15 nm was used. According to these calculations, which are summarized in Figure 4A, the “more volatile” particles are $>97\%$ volatile material, and the volatile volume fraction of “less volatile” particles decreases monotonically as the size increases, from $\sim 90\%$ at 30 nm to $\sim 5\%$ at 200 nm. Figure 4B shows results of similar analyses for the measurements with CA fuel at 35% load, for which the volatile volume fractions were lower than those at 20% load.

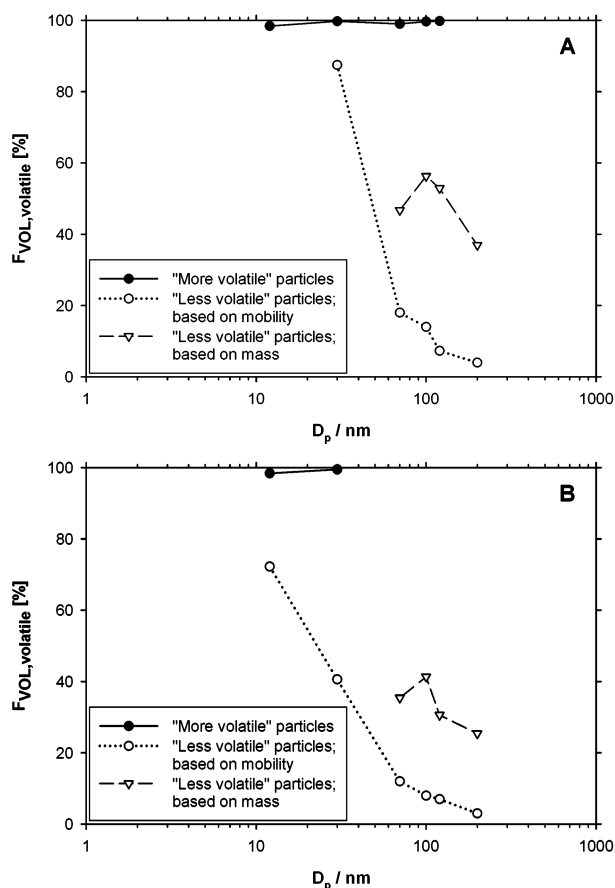


FIGURE 4. Volume fractions of volatile components in “more volatile” and “less volatile” diesel particles and comparison between the TDMA and TDMA–APM methods for determining volatile volume fractions of “less volatile” particles. In both plots the data were obtained with CA fuel and the engine load was (A) 20% and (B) 35%.

In the second method, the volatile volume fraction ($F_{VOL,volatile}^{APM}$) was calculated from the mass change determined by the Long TDMA–APM using the following equations:

$$F_{VOL,volatile}^{APM} = \frac{1}{1 - \frac{\rho_{volatile}}{\rho_{nonvolatile}} \left(1 - \frac{1}{F_{MASS,volatile}^{APM}} \right)} \quad (4)$$

where

$$F_{MASS,volatile}^{APM} = \frac{m_{p,initial} - m_{p,nonvolatile}}{m_{p,initial}} \quad (5)$$

$\rho_{volatile}$ and $\rho_{nonvolatile}$ are the densities of volatile and nonvolatile material, respectively; $F_{MASS,volatile}^{APM}$ is the mass fraction of volatile material; and $m_{p,initial}$ and $m_{p,nonvolatile}$ are the particle masses determined by the Long TDMA–APM before and after heating, respectively. The density of volatile material was assumed to be $0.8 \times 10^3 \text{ kg m}^{-3}$, equal to the material density of the major class of hydrocarbons in engine oil (branched and cyclic alkanes), which was found to be the major volatile constituent of diesel particles (17). The density of nonvolatile material was assumed to be $2 \times 10^3 \text{ kg m}^{-3}$, equal to that of amorphous elemental carbon because the major nonvolatile constituent is considered to be soot (10). The mass measurements were made on “less volatile” particles with initial diameters of 70, 100, 120, and 200 nm at a fixed heater temperature of 110 °C. At 20% load, the masses before heating were 1.70×10^{-19} , 4.75×10^{-19} ,

7.47×10^{-19} , and 2.44×10^{-18} kg, and those after heating were 1.26×10^{-19} , 3.14×10^{-19} , 5.15×10^{-19} , and 1.98×10^{-18} kg at 70, 100, 120, and 200 nm, respectively. These give the volatile mass fractions ($F_{\text{MASS,volatile}}^{\text{APM}}$) of 0.26, 0.34, 0.31, and 0.19 at 70, 100, 120, and 200 nm, respectively. The volatile volume fractions calculated from these mass measurements are plotted in Figure 4 for comparison with the results from the TDMA-based technique. The volatile volume fractions obtained from mass measurements were 40–60% and 25–40% at loads of 20% and 35%, respectively, significantly higher than those from mobility measurements. We attribute this difference to evaporation of volatile material from the interstitial spaces of highly irregularly shaped particles, which leads to changes in particle mass but minimal changes in particle shape and mobility.

For diesel chain agglomerates, the volatile volume fraction is therefore determined far more accurately by using the method based on mass changes. Furthermore, the discrepancy appears to become worse as the particle diameter increases. For the results shown in Figure 4, the ratio of the volatile volume fractions calculated from mobility and mass measurements decreased from ~ 0.3 at 70 nm to ~ 0.1 at 200 nm. This apparently occurred because the particle shape became more irregular with increasing size. This can be demonstrated by calculating the “effective densities” of the nonvolatile particles that remain after heating, using the equation

$$\rho_{\text{eff,nonvolatile}} = \frac{6m_{\text{p,nonvolatile}}}{\pi(D_{\text{p,nonvolatile}}^{\text{TDMA}})^3} \quad (6)$$

For irregularly shaped particles, the effective density is less than the true density (i.e., mass/volume in the absence of pore space) (31). At 20% load, the effective densities were 0.86×10^3 , 0.71×10^3 , 0.62×10^3 , and 0.49×10^3 kg m $^{-3}$ for 70-, 100-, 120-, and 200-nm particles, respectively. Assuming that the nonvolatile residual particles were composed solely of elemental carbon and that the true particle density was equal to the material density of elemental carbon (2×10^3 kg m $^{-3}$), these values indicate that the effective density decreased from $\sim 45\%$ to $\sim 25\%$ of the true density due to increasing irregularity in particle shape as the particle size increases.

We also found that the effective densities of the “less volatile” particles decreased upon heating. The effective densities before heating were calculated for the same particle sizes using the equation

$$\rho_{\text{eff,initial}} = \frac{6m_{\text{p,initial}}}{\pi(D_{\text{p,initial}}^{\text{TDMA}})^3} \quad (7)$$

The values were 0.95×10^3 , 0.93×10^3 , 0.84×10^3 , and 0.58×10^3 kg m $^{-3}$, which were all slightly larger than those calculated above for the heated particles. Although true particle densities must have increased upon heating due to the loss of low-density organics, particle shapes must have become more irregular, resulting in a net reduction in the effective densities. It should be noted that Park et al. (38) observed that the effective density of diesel exhaust particles was greater at a lower engine load. They hypothesized that, at lower engine loads, more semivolatile hydrocarbons were present in engine exhaust resulting in more condensation of hydrocarbons onto soot agglomerates, which made the shape of the agglomerates more compact and hence increased the effective density. Our observation, which inferred that the particle shape became more irregular when volatile material was driven off, supports this hypothesis.

The volatile volume fraction determined for “less volatile” particles by the Long TDMA–APM has a maximum at 100

nm for both engine loads, as shown in Figure 4. Although mass measurements were not made for particles smaller than 70 nm, previous studies by electron microscopy show that particles become more spherical with decreasing size (38). Therefore, the volatile volume fraction of “less volatile” particles calculated from mobility measurements should become more accurate. The volatile volume fraction of “less volatile” particles should therefore increase as the size decreases from 70 to 30 nm, assuming that the 30-nm particles were spherical. This means that, in addition to the maximum at 100 nm, the volatile volume fraction of “less volatile” particles has a local minimum between 30 and 100 nm. The reason for this complicated structure is not yet known but may be related to the greater agglomeration and interstitial volume of larger “less volatile” particles.

Mass Distributions of Volatile and Nonvolatile Compounds. From our analysis of the size-dependent mixing ratios and mass fractions of volatile and nonvolatile material in diesel exhaust aerosols, we can calculate the size-segregated mass contribution of (a) nonvolatile components in “less volatile” particles, (b) volatile components in “less volatile” particles, and (c) volatile components in “more volatile” particles. The mass concentrations of the three components were calculated at each mobility diameter as

$$\frac{dM_{(a)}}{d \log D_p} = \frac{dN_{\text{total}}}{d \log D_p} (1 - F_{\text{NUM,“more volatile”}}) m_{\text{p,nonvolatile}} \quad (8)$$

$$\frac{dM_{(b)}}{d \log D_p} = \frac{dN_{\text{total}}}{d \log D_p} (1 - F_{\text{NUM,“more volatile”}}) (m_{\text{p,init}} - m_{\text{p,nonvolatile}}) \quad (9)$$

$$\frac{dM_{(c)}}{d \log D_p} = \frac{dN_{\text{“more volatile”}}}{d \log D_p} \rho_{\text{volatile}} \frac{\pi D_p^3}{6} \quad (10)$$

where $dN_{\text{total}}/d \log D_p$ is the number-weighted size distribution function shown in Figure 1 obtained by the SMPSSs. Since we could not carry out mass measurements for “more volatile” particles (below the APM size limit), their mass concentrations were calculated by assuming a spherical shape and absolute density of 0.8×10^3 kg m $^{-3}$ for volatile material (i.e., organics) and the log-normal number-weighted size distribution function used to fit the nuclei mode in Figure 1 ($dN_{\text{“more volatile”}}/d \log D_p$). The results are summarized in Figure 5 for the CA fuel at 20% and 35% loads. At 20% load (Figure 5A), volatile material was distributed across a wide range of particle sizes that included both the nuclei and accumulation modes. It appears that the volatile mass concentration in the accumulation mode is significant. The estimate based on TDMA measurements (mobility-based) would be very different since the calculated volume fractions of volatile material in the accumulation mode were underestimated by ~ 70 – 90% as demonstrated in the previous section. The contribution of the nuclei mode almost totally disappears for the CA fuel at 35% load (Figure 5B), so that the total volatile mass is dominated by the accumulation mode. The difference in partitioning of volatile material between the nuclei and accumulation modes at the two engine loads is a reflection of less favorable conditions for formation of a nuclei mode at the higher engine load, i.e., higher exhaust temperatures that favor oxidation of volatile material in the exhaust and reduce the saturation ratio during dilution and the larger surface area provided by nonvolatile cores of the “less volatile” particles.

Overall, the plots in Figure 5 show how the masses of volatile and nonvolatile components are distributed while those in Figure 1 provide the number-weighted distributions

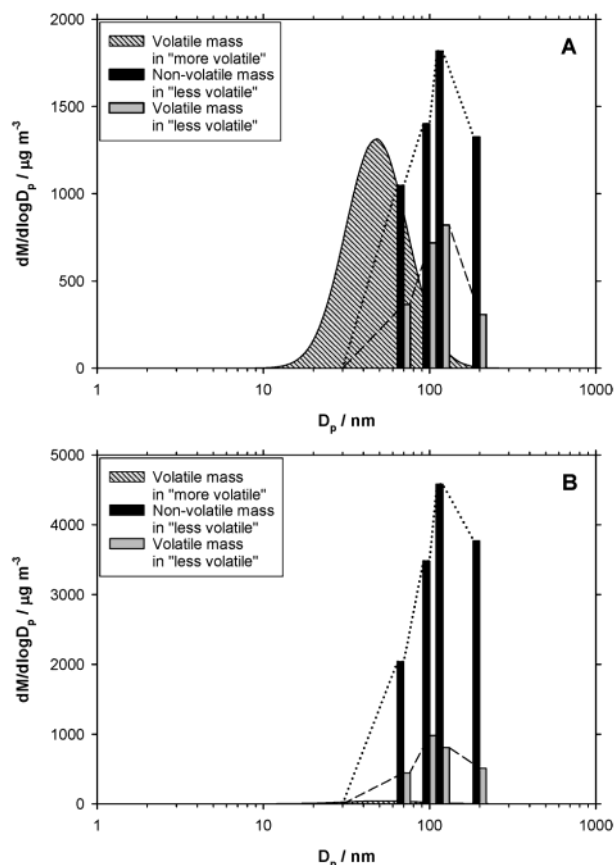


FIGURE 5. Mass distributions of volatile and nonvolatile components in diesel particles formed with the engine operating on CA fuel at (A) 20% and (B) 35% load. The volatile mass distribution of "more volatile" particles is represented by the gray area under the log-normal curve, while the volatile and nonvolatile masses of "less volatile" particles are shown as bars.

of the two types of particles with different volatilities. The information given by these plots would be useful where accurate characterization of the mixing state of diesel exhaust aerosols is essential, such as in exposure experiments in health effects studies and in studies for emission control.

Acknowledgments

We are grateful to the Coordinating Research Council and the California Air Resources Board for funding this research, which is co-sponsored by the Engine Manufacturers Association, Southcoast Air Quality Management District, Cummins, Caterpillar, and Volvo. Construction of the Nano TDMA was supported financially by the U.S. Department of Energy through Grant DE-FG02-98ER62556. The Long TDMA-APM measurements were supported by the U.S. Environmental Protection Agency through Grant R 826372-01-0 to the Georgia Institute of Technology and GIT Subcontract G-35-W62-G1 to the University of Minnesota. This work has not been subjected to the Agency's required peer and policy review and therefore does not necessarily reflect the views of the Agency, and no official endorsement should be inferred. We also acknowledge support from NSF Grant NSF/ATM-0096555. We thank Robert W. Waytulonis, Tom M. Jones, Kris H. Koenig, and Michael F. McTigue of the Center for Diesel Research of the University of Minnesota for assistance during engine measurements.

Supporting Information Available

One figure. This material is available free of charge via the Internet at <http://pubs.acs.org>.

Literature Cited

- (1) Pope, C. A., III.; Thun, M. J.; Namboodiri, M. M.; Dockery, D. W.; Evans, J. S.; Speizer, F. E.; Heath, C. W., Jr. *Am. J. Respir. Crit. Care Med.* **1995**, *151*, 669–674.
- (2) Seaton, A.; MacNee, W.; Donaldson, K.; Godden, D. *Lancet* **1995**, *345*, 176–178.
- (3) Dockery, D. W.; Pope, C. A.; Xu, X.; Spengler, J. D.; Ware, J. H.; Fay, M. E.; Ferris, B. G.; Speizer, F. E. *N. Engl. J. Med.* **1993**, *329*, 1753–1759.
- (4) National Research Council. *Research priorities for airborne particulate matter: I. Immediate priorities and a long-range research portfolio*; National Academy Press: Washington, DC, 1998.
- (5) Health Effects Institute. *Understanding the health effects of components of the particulate matter mix: Progress and next steps*; Health Effects Institute: Cambridge, MA, 2002.
- (6) Mauderly, J. L.; Ness, L.; Schlesinger, R. In *Atmospheric observations: Helping build the scientific basis for decisions related to airborne particulate matter*; Albritton, D. L., Greenbaum, D. S., Eds.; Health Effects Institute: Cambridge, MA, 1998; pp 9–14.
- (7) U.S. Environmental Protection Agency. *Health assessment document for diesel engine exhaust*; U.S. Government Printing Office: Washington, DC, 2002.
- (8) Health Effects Institute. *Research directions to improve estimates of human exposure and risk from diesel exhaust*; Health Effects Institute: Cambridge, MA, 2002.
- (9) California Environmental Protection Agency. *Proposed identification of diesel exhaust as a toxic air contaminant. Part B. Health risk assessment for diesel exhaust*; Sacramento, CA, 1998 [ftp://ftp.arb.ca.gov/carbis/regact/diesltac/partb.pdf](http://ftp.arb.ca.gov/carbis/regact/diesltac/partb.pdf).
- (10) Kittelson, D. B. *J. Aerosol Sci.* **1998**, *29*, 575–588.
- (11) Kittelson, D. B.; Johnson, J.; Watts, W.; Wei, Q.; Drayton, M.; Paulsen, D.; Bukowiecki, N. *SAE Tech. Pap. Ser.* **2000**, No. 2000-01-2212.
- (12) Abdul-Khalek, I.; Kittelson, D.; Brear, F. *SAE Tech. Pap. Ser.* **1999**, No. 1999-01-1142.
- (13) Schauer, J. J.; Kleeman, M. J.; Cass, G. R.; Simoneit, B. R. T. *Environ. Sci. Technol.* **1999**, *33*, 1578–1587.
- (14) Abdul-Khalek, I. S.; Kittelson, D. B. *SAE Tech. Pap. Ser.* **1995**, No. 950236.
- (15) Maricq, M. M.; Chase, R. E.; Xu, N.; Laing, P. M. *Environ. Sci. Technol.* **2002**, *36*, 283–289.
- (16) Matter, U.; Siegmann, H. C.; Burtcher, H. *Environ. Sci. Technol.* **1999**, *33*, 1946–1952.
- (17) Sakurai, H.; Tobias, H. J.; Park, K.; Zarling, D.; Docherty, K. S.; Kittelson, D. B.; McMurry, P. H.; Ziemann, P. *J. Atmos. Environ.* **2003**, *37*, 1199–1210.
- (18) Lee, D.; Miller, A. L.; Kittelson, D. B.; Zachariah, M. R. Manuscript in preparation.
- (19) Jung, H.; Kittelson, D. B.; Zachariah, M. R. Manuscript in preparation.
- (20) Abdul-Khalek, I. S.; Kittelson, D. B.; Graskow, B. R.; Wei, Q.; Brear, F. *SAE Tech. Pap. Ser.* **1998**, No. 980525.
- (21) Abdul-Khalek, I. S.; Kittelson, D. B.; Brear, F. *SAE Tech. Pap. Ser.* **1998**, No. 982599.
- (22) Du, C. J.; Kracklauer, J.; Kittelson, D. B. *SAE Tech. Pap. Ser.* **1998**, No. 980536; *SAE Trans., J. Fuels Lubr.* **1998**, No. SP-1326.
- (23) Zhang, S.-H.; Seinfeld, J. H.; Flagan, R. C. *Aerosol Sci. Technol.* **1993**, *19*, 3–14.
- (24) Orsini, D. A.; Wiedensohler, A.; Stratmann, F.; Covert, D. S. *J. Atmos. Ocean. Technol.* **1999**, *16*, 760–772.
- (25) Brooks, B. J.; Smith, M. H.; Hill, M. K.; O'Dowd, C. D. *J. Aerosol Sci.* **2002**, *33*, 555–579.
- (26) Schmid, O.; Eimer, B.; Hagen, D. E.; Whitefield, P. D. *Aerosol Sci. Technol.* **2002**, *36*, 877–889.
- (27) Philippin, S.; Stratmann, F.; Wiedensohler, A. *J. Aerosol Sci.* **1999**, *30*, S117–S118.
- (28) Kwon, S.-B.; Lee, K. W.; Saito, K.; Shinozaki, O.; Seto, T. *Environ. Sci. Technol.* **2003**, *37*, 1794–1802.
- (29) Burtcher, H.; Baltensperger, U.; Bukowiecki, N.; Cohn, P.; Hüglin, C.; Mohr, M.; Matter, U.; Nyeki, S.; Schmatloch, V.; Streit, N.; Weingartner, E. *J. Aerosol Sci.* **2001**, *32*, 427–442.
- (30) Ehara, K.; Hagwood, C.; Coakley, K. J. *J. Aerosol Sci.* **1996**, *27*, 217–234.
- (31) McMurry, P. H.; Wang, X.; Park, K.; Ehara, K. *Aerosol Sci. Technol.* **2002**, *36*, 227–238.
- (32) Wang, S. C.; Flagan, R. C. *Aerosol Sci. Technol.* **1990**, *13*, 230–240.

- (33) Knutson, E. O.; Whitby, K. T. *J. Aerosol Sci.* **1975**, *6*, 443–451.
- (34) Liu, B. Y. H.; Pui, D. Y. H. *J. Colloid Interface Sci.* **1974**, *47*, 155–171.
- (35) Chen, D.-R.; Pui, D. Y. H.; Hummes, D.; Fissan, H.; Quant, F. R.; Sem, G. J. *J. Aerosol Sci.* **1997**, *29*, 497–509.
- (36) Stolzenburg, M. R.; McMurry, P. H. *Aerosol Sci. Technol.* **1991**, *14*, 48–65.
- (37) Wehner, B.; Philippin, S.; Wiedensohler, A. *J. Aerosol Sci.* **2002**, *33*, 1087–1093.
- (38) Park, K.; Cao, F.; Kittelson, D. B.; McMurry, P. H. *Environ. Sci. Technol.* **2003**, *37*, 577–583.
- (39) Stolzenburg, M. R. Ph.D. Thesis, University of Minnesota, Minneapolis, MN, 1988.
- (40) Kousaka, Y.; Okuyama, K.; Adachi, M.; Mimura, T. *J. Chem. Eng. Jpn.* **1986**, *19*, 401–407.
- (41) Kesten, J.; Reineking, A.; Porstendörfer, J. *Aerosol Sci. Technol.* **1991**, *15*, 107–111.
- (42) Zhang, Z.; Liu, B. Y. H. *Aerosol Sci. Technol.* **1991**, *15*, 228–238.
- (43) Stratmann, F.; Kauffeldt, T.; Hummes, D.; Fissan, H. *Aerosol Sci. Technol.* **1997**, *26*, 368–383.
- (44) Rader, D. J.; McMurry, P. H. *J. Aerosol Sci.* **1986**, *17*, 771–787.
- (45) Stolzenburg, M. R.; McMurry, P. H. *TDMAFIT user's manual*; Particle Technology Laboratory, University of Minnesota: Minneapolis, MN, 1988.
- (46) Stratmann, F.; Orsini, D.; Kauffeldt, T. *J. Aerosol Sci.* **1997**, *28*, S701–S702.
- (47) Voutilainen, A.; Stratmann, F.; Kaipio, J. P. *J. Aerosol Sci.* **2000**, *31*, 1433–1445.
- (48) Markowski, G. R. *Aerosol Sci. Technol.* **1987**, *7*, 127–141.
- (49) Higgins, K. J.; Jung, H.; Kittelson, D. B.; Roberts, J. T.; Zachariah, M. R. *J. Phys. Chem. A* **2002**, *106*, 96–103.
- (50) Harris, S. J.; Maricq, M. M. *J. Aerosol Sci.* **2001**, *32*, 749–764.
- (51) Wei, Q.; Kittelson, D. B.; Watts, W. F. *SAE Tech. Pap. Ser.* **2001**, No. 2001-01-0201.
- (52) Lemmon, E. W.; Goodwin, A. R. H. *J. Phys. Chem. Ref. Data* **2000**, *29*, 1–39.

Received for review April 17, 2003. Revised manuscript received September 10, 2003. Accepted September 17, 2003.

ES034362T